Driving Range Extension of a PV Array Fed Anti-Windup and MTPA Controlled PMaSyRM Drive for LEV With Regeneration

Sushant KUMAR, Shailendra KUMAR, and Shashank KURM

***Abstract*—This paper presents a permanent magnet assisted synchronous reluctance motor driven light electric vehicle integrated with solar photovoltaic (SPV) panels and battery storage. The proposed system leverages regenerative braking and energy harvesting from rooftop mounted SPV to extend the driving range, contributing significantly to green mobility. A bidirectional DC-DC converter (BDDC) is employed to facilitate energy flow between the battery and the motor drive in either direction. During regenerative braking, the kinetic energy of the PMaSyRM drive-based vehicle is converted into electrical energy. This recovered energy is injected into the battery, effectively charging the battery. This process not only extends the driving range of the vehicle but also minimizes energy loss, thereby enhancing overall efficiency. The conditional integrator-based anti-windup technique is employed for the speed control of LEV, which eliminates the problem of ringing and overshooting during the speed transitions. For better torque control of the PMaSyRM, maximum torque per ampere (MTPA) technique is used. Based on the torque command, MTPA technique produces set of current commands to minimize the magnitude of current vector. Constant voltage, current and torque curve study of the PMaSyRM assures that current and voltage of the drive remains in the safe limit.**

***Index Terms*—Anti-windup technique, bi-directional DC-DC converter, light electric vehicle (LEV), maximum torque per ampere, permanent magnet assisted synchronous reluctance machine (PMaSyRM), solar photovoltaic (SPV).**

I. Introduction

In response to the environmental challenges posed by carbon emissions from IC engine-based vehicles, research on electric vehicles (EVs) has gained momentum [1]−[2]. A key challenge lies in reducing cost of EVs, size, and charging time of the battery [3]−[5]. Charging from sustainable and green power sources is crucial for enhancing EV sustainability, making solar photovoltaic (PV) arrays a promising option for future EV battery charging [6]. In recent years, global production of battery-powered EVs has surged. However, EVs still face significant challenges, including inadequate charging infrastructure, frequent battery replacement, and limited driving range. The primary focus is on designing EV drive systems efficiently to maximize the per-charge driving range of light electric vehicles (LEVs) [7]−[8].

The driving range is the distance that can be travelled by the EVs with the available battery capacity. The driving range of an EV depends upon factors related to the speed or acceleration. These factors are positive or negative maximum speed and acceleration, range of speed, time taken by the EV to accelerate or decelerate and the driving cycle. The details of vehicles based on the calculations from vehicle dynamics and driving-related dynamics modeling, various driving cycles, and other aspects of EVs are discussed in [9]−[10]. The cycles and the driving range of the EV are determined. The driving range of EVs is constrained by battery capacity. Utilizing higher capacity batteries in EVs may result in an increment in the cost and weight of the EVs. During braking of the EVs, recovery of kinetic energy from the wheels is a viable solution to increase the life cycle of the battery and driving range of LEV. Charing of the battery from regenerative braking is possible, as presented in [11]−[12]. One of the effective control methods to recover regenerative energy during braking is the bidirectional DC-DC converter (BDDC) control system [13]−[15]. A Li-ion battery is used to power LEV in the proposed system. Li-ion batteries offer a higher depth of discharge as compared to other types of batteries, making them more cost-effective in the long run. Under various weather conditions, the continuous operation of LEV is ensured by the integration of an SPV with the Li-ion battery. The SPV panel mounted on rooftop charges the battery during non-operation hours of LEV. The perturb and observe (P&O) MPPT algorithm is employed for tracking the maximum power point from the SPV source [16]. Recent research indicates that, for EV and HEV applications synchronous reluctance machines (SyRM) has a significant edge over other motors [17]−[18].

Asynchronous motor-based drives such as induction motor drives (IMD) are the most widely used drives for EV applications. The permanent magnet-based drives such as PMSM, and BLDC drives are also the most widely used for EV applications. A comparison of IMDs with PMSMs for EV application is given

Manuscript received October 27, 2024; revised December 31, 2024; accepted February 16, 2025. Date of publication March 30, 2025; date of current version February 28, 2025. No funding was received to assist with the preparation of this manuscript. *(Corresponding author: Shailendra Kumar.)*

All authors are with Electrical Engineering Department of Electrical Engineering, Indian Institute of Technology Bhilai, Chhattisgarh 491001, India (e-mail: sushantk@iitbhilai.ac.in; skumaree@iitbhilai.ac.in; kurmshashank@iitbhilai.ac.in).

Digital Object Identifier 10.24295/CPSSTPEA.2025.00007

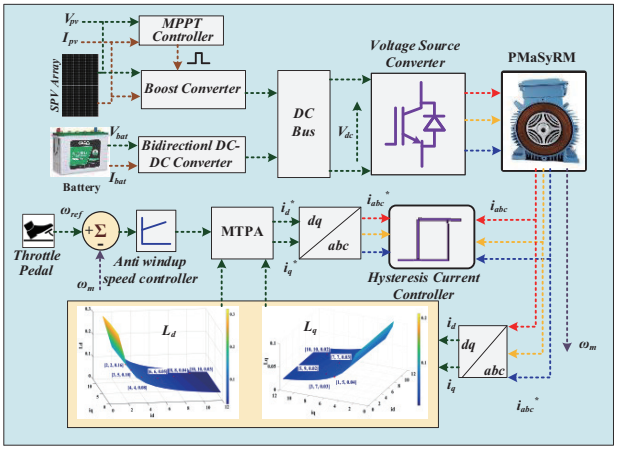

Fig. 1. General configuration of proposed regenerative braking scheme with roof-top mounted SPV and PMaSyRM-based LEV.

in [19]. SyRM machines offer distinct advantages in terms of their construction and low cost. The simple design of the rotor, absence of permanent magnets, negligible cogging torque, and reliable performance are some of the advantages discussed in [20]. Consequently, they are well-positioned to replace other motors in EV applications. SyRMs are more efficient than IMs and on par with PMSMs [21]. However, SyRM machines suffer from low power factor. To counter this drawback, low-cost ferrite PMs can be provided in the rotor construction of SyRMs. These types of SyRMs are known as permanent magnet-assisted synchronous reluctance machines (PMaSyRM). The introduction of PMs increases the power factor, efficiency, and torque density and reduces the ohmic losses in the machine. It also reduces the size and weight of the machine as compared to same rating of SyRM. The major advantage of PMaSyRM is that it can produce torque due to both permanent magnets and reluctance property of the machine. However, for optimized production of the torque it is important that machine should operate within the current and voltage rating of the machine and inverters [22].

MTPA is the technique introduced in [23], which produces *d* and *q* axis reference current set based on the reference torque to keep the current vector inside its operating limit. Look-up table for *d* and *q* axis inductance values is the most widely used method for current set generation in IPMSMs. Hence for optimal production of torque in PMaSyRM, look-up table is advantageous. Electric machines used in EV applications encounter varying speed and torque conditions during the driving cycle, including acceleration, cruising, and deceleration modes. Hence, an anti-windup-based vector control technique is used to control the speed of the SYRM drive. In the vector control technique, a PI controller is used to track the reference speed. However, the problem with the conventional PI controller is the integrator windup phenomenon. The windup activity in the integrator observes when the PI controller output is saturated and large changes in the set point are made. Integrator windup leads to deterioration in the closed-loop performance of the PI controller. The deterioration here is referred to as degradation in the control performance and high overshoot. Hence, to counter the windup phenomenon, the anti-windup technique is used. Anti-windup technique for the induction motor drives is discussed in [24], and for PMSM drives is discussed in [25]. Based on the method used, anti-windup techniques are classified as limited type integrator, tracking back calculation based and conditional integration, which utilizes a dead zone operator. The conditional integral-based technique ensures zero steady-state error. In the case of conditional integral-based anti-wind-up technique, integration is switched on or off based on the control error. For vehicular applications, the PMaSyRM drive is employed for dynamic control across different operating modes [26]–[28].

The major contributions of the proposed work are, rooftop mounted PV panels aids to utilize the solar energy and reduces the dependency on the grid for battery charging, BDDC extract the previously wasted power during braking and charges the battery to improve the range of the LEV, implementation of robust anti-windup PI controller improves the stability and dynamic performance of the PMaSyRM under varying load conditions, MTPA technique optimizes the efficiency of the PMaSyRM and ensures minimum losses during operation. A comprehensive analysis is conducted to study the efficiency of the proposed system through experimental validation. Also, conducted comprehensive cost comparison analysis with the existing LEVs. The proposed roof-top SPV-mounted LEV system is modeled in MATLAB/Simulink and evaluated for accelerating, cruising, and braking operation of LEV. The proposed work is structured as follows: Section II describes the general configuration of the proposed system, Section III describes the overall control technique of system, Section IV presents the simulated performance for acceleration, cruising, and braking operation of the LEV, including an estimation of the driving range, Experimental results are presented in Section V, followed by conclusions in Section VI.

II. System Architecture

Fig. 1 shows a general configuration of the proposed work for SPV and battery-integrated PMaSyRM drive for LEVs. It comprises an LEV powered by a 1.5 kW, 230 V PMaSyRM drive, and a 240 V, 42 Ah battery with a BDDC. The battery is charged using the power generated by the SPV installed at the rooftop of the LEV whenever solar irradiance is available. The P&O algorithm is used to harness the peak power from the SPV panel. The BDDC control system and the battery maintain the DC link voltage. Parameters of rooftop SPV, boost converter and BDDC are mentioned in Appendices.

III. Control Technique of Proposed LEV

This section explains the control strategy for the proposed PMaSyRM drive-based LEV powered by a roof-top mounted SPV and battery. The DC link voltage is maintained by the BDDC. Motoring and regenerative actions of the drive is controlled by BDDC. The efficiency of the LEV is improved with regenerative braking as the energy is supplied back to the battery for its charging. For independent torque and flux

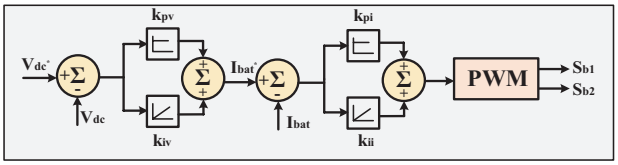

Fig. 2. Bidirectional DC-DC controller topology.

control of PMaSyRM, vector control with an anti-windup technique and maximum torque per ampere (MTPA) is applied. Vector control with anti-windup and MTPA produces reference *dq* axis current components i_{ds}^* and i_{qs}^* of winding currents. Inverse Park's transform is used to evaluate the three-phase reference winding currents. These reference signals are given to the hysteresis current controller along with the sensed winding currents to produce gating signals for the three-voltage source inverter (VSI). Fig. 2 presents the controller topology for BDDC [29].

A. Mathematical Model of PMaSyRM and Anti-Windup FOC

In the *dq* synchronous rotating reference frame, the dynamic model of the PMaSyRM is given below:

$$\frac{\mathrm{d}i_d}{\mathrm{d}t} = \frac{v_d}{L_d} - \frac{R_s}{L_d} i_d + \frac{\omega_e L_q i_q}{L_d} \tag{1}$$

$$\frac{\mathrm{d}i_q}{\mathrm{d}t} = \frac{v_q}{L_q} - \frac{R_s}{L_q} i_q - \frac{\omega_e L_d i_d}{L_q} - \frac{\omega_e \lambda_{PM}}{L_q} \tag{2}$$

$$\frac{\mathrm{d}\omega_e}{\mathrm{d}t} = \frac{2}{J \times P} T_e - \frac{2}{J \times P} T_L \tag{3}$$

where R_s is stator resistance, L_d and L_q are the *dq* axis inductance values of the PMaSyRM. v_{dq} and i_{dq} represent the voltage and current in a *dq* synchronous rotating reference frame respectively. λ_{PM} is the flux linkage due to the permanent magnet, ω_e is the electrical speed of the PMaSyRM and P is the number of poles of the machine. J is the moment of inertia of the machine. T_e and T_L are the electromagnetic torque and load torque of the machine.

In the proposed work the anti-windup PI controller processes the error between the reference speed and actual measured speed to produce reference value of the electromagnetic torque. From this reference value of the electromagnetic torque, reference values of stator current components i_d^* and i_q^* are generated. For the generation of the i_d^* and i_q^*, MTPA technique is used. MTPA technique ensures that machine should be able to produce the required electromagnetic torque. MTPA technique also ensures that the *d* and *q* axis components of stator currents should be distributed such that, the resultant stator current is minimized. This ensures that the required torque is produced by the machine with minimum possible stator currents. Fig. 3 presents the MTPA line, voltage limit ellipse, current limit circle and torque limit curve of the PMaSyRM at rated speed and toque value. If the value of the DC link voltage is well within the limit of the machine rating,

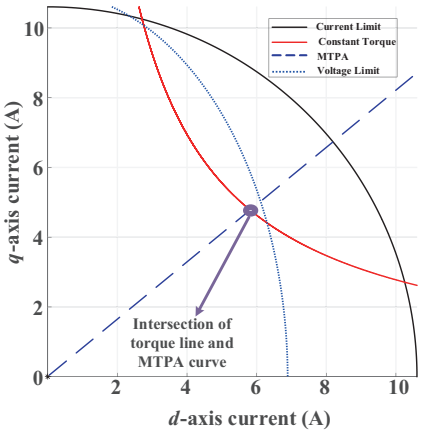

Fig. 3. Voltage limit ellipse, current limit circle, constant torque plot and MTPA plot of PMaSyRM.

then it is expected that machine should operate at or near the intersection point of the constant torque curve and MTPA line. The tentative operating point for rated speed and torque is shown in Fig. 3. The electromagnetic torque produced by the PMaSyRM is given by

$$T_e = \frac{3}{2}\frac{P}{2}[\lambda_{PM} + (L_d - L_q) i_d] i_q \tag{4}$$

By neglecting voltage drop across R_s, the voltage and current limits are expressed as

$$L_d^2 \left(i_d + \frac{\lambda_m}{L_d} \right)^2 + L_q^2 i_q^2 \leq \frac{V_s^2}{\omega_e} \tag{5}$$

$$i_d^2 + i_q^2 \leq I_s^2 \tag{6}$$

where V_s is the peak value of the phase voltage and I_s is the peak value of the winding current.

From (4) it is observed that PMaSyRM can produce both reluctance torque and torque due to permanent magnets. MTPA is the technique to utilize both torques optimally. To achieve maximum developed torque within the rated speed of a PMaSyRM, the reference *d*-axis current value must be kept to its optimal value. This value is determined by the characteristics of the machine. The value of the current is determined by modeling the motor and constrained minimization technique

$$L_d^2 \left(i_d + \frac{\lambda_{PM}}{L_d} \right)^2 + (L_q^2 i_q^2) \leq \frac{V_s}{\omega_e^2} \tag{7}$$

Minimize

$$i_d^2 + i_q^2 \tag{8}$$

Subject to

$$\frac{3}{2}\frac{P}{2}[\lambda_{\mathrm{PM}}+(L_d-L_q)i_d]i_q=T_{\mathrm{L}} \tag{9}$$

Hence in the context of reference torque, (8) and (9) can be modified as,

Minimize

$$i_d^{*2}+i_q^{*2} \tag{10}$$

Subject to

$$\frac{3}{2}\frac{P}{2}[\lambda_{\mathrm{PM}}+(L_d-L_q)i_d^{*}]i_q^{*}=T_{\mathrm{em}}^{*} \tag{11}$$

where * represents the reference values of the variables. In place of load torque T_{L}, T_{em}^{*} is now being considered. That is the reference torque has to be produced by the machine by minimizing the reference currents. (10) and (11) form a problem, that can be converted into an auxiliary function by introducing a Lagrangian multiplier ζ. The functional problem is expressed as follows

$$F=\sqrt{i_d^{*2}+i_q^{*2}}+\zeta\left\{T_{\mathrm{em}}^{*}-\frac{3P}{4}\left[\lambda_{\mathrm{pm}}i_d^{*}+(L_d-L_q)i_d^{*}i_q^{*}\right]\right\} \tag{12}$$

In solving thess equation, the values of i_d^{*} and i_q^{*} are calculated as follows

$$i_d^{*}=\frac{\lambda_{\mathrm{m}}\pm\sqrt{\lambda_{\mathrm{m}}^{2}+8I^{2}(L_q-L_d)^{2}}}{4(L_d-L_q)} \tag{13}$$

$$i_q^{*}=\frac{T_{\mathrm{em}}^{*}}{3P/4[\lambda_{\mathrm{pm}}+(L_d-L_q)i_d]} \tag{14}$$

It is observed that for the implementation of the MTPA technique, reference currents are calculated from the reference torque and minimized, to keep the current within the inverter and machine constraints, that is the current rating of the inverter and the machine. These reference currents are then transformed to three-phase reference currents, which are then compared with the actually measured currents of the machine in the hysteresis current controller to produce the pulses for the switching operation of the VSC.

L_d, L_q are saturated values of dq-axis inductances. But in the running condition of the PMaSyRM, it is difficult to measure L_{dq}. Hence in the running condition of the motor L_{dq} can be computed by an indirect method. Under the rated condition the value L_{dq} can be computed as follows

$$L_d(i_d,i_q)=\frac{V_q-E_0+Ri_q}{\omega_{\mathrm{e}}i_d} \tag{15}$$

$$L_q(i_d,i_q)=\frac{V_d-Ri_d}{\omega_{\mathrm{e}}i_q} \tag{16}$$

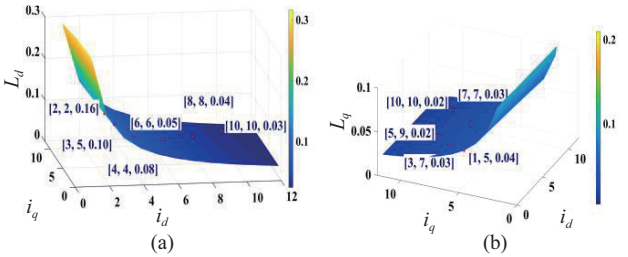

(a) (b)

Fig. 4. Variations in inductance values with currents (a) L_d, (b) L_q.

where E_0 is the electromotive force at no load condition and V_d and V_q are the stator voltage component along the d and q axis respectively. Fig. 4 presents the 3D plots of variations in L_d and L_q with respect to i_d and i_q. As it is observed in Fig. 4(a)-(b), for selected sampled values of i_d and i_q, there are corresponding values of L_d and L_q. Similarly, for different values of i_d and i_q, corresponding values of L_d and L_q are recorded from the plots. This process creates a range of values of L_d and L_q, for possible ranges of stator currents. The look-up table also interpolates for the intermediate values of i_d and i_q. Then, a look-up table is formed using the recorded values. The currents measured from the stator terminals of PMaSyRM are converted into the dq axes currents using the park transformation. The transformed currents are then passed through the corresponding look-up tables to finalize the L_d and L_q values.

As shown in Fig. 3, the voltage limit ellipse is presented as a dotted ellipse in dq axis current plane. The center of the ellipse is ($-\lambda_{\mathrm{PM}}/L_d$,0). The major and minor axis radii of the ellipse are inversely proportional to the speed. This shows that whenever the speed of the PMaSyRM increases, the ellipse will shrink. The current limit is presented as a circle. The center of the circle is at the origin whereas, the radius of the circle is the maximum rated current of the PMaSyRM. The winding current satisfying both the voltage and current constraint of (10) and (11) must lie inside the voltage limit ellipse and current limit circle shown in Fig. 3.

B. Speed Controller with Integrator Anti-Windup Technique

The PMaSyRM drive is considered as a first-order system and the transfer function of the LEV is expressed as

$$\frac{\mathrm{d}\omega_{\mathrm{m}}}{\mathrm{d}t}=-\frac{\omega_{\mathrm{m}}\cdot B}{J_{\mathrm{m}}}+\frac{T_{\mathrm{e}}^{*}}{J_{\mathrm{m}}}-\frac{T_{\mathrm{l}}}{J_{\mathrm{m}}} \tag{17}$$

where J_{m} is the moment of inertia and B is the viscous friction of the PMaSyRM. T_{l} is the load torque applied to the PMaSyRM Based LEV. It is considered that the controlled input v to the LEV is limited by the saturation. Saturation is a type of non-linearity, which is expressed as

$$v=\begin{cases}U_{\mathrm{h}} & u>U_{\mathrm{h}}\\ u & U_{\mathrm{l}}\leqslant u\leqslant U_{\mathrm{h}}\\ U_{\mathrm{l}} & u<U_{\mathrm{l}}\end{cases} \tag{18}$$

where u is the controller output. U_h and U_l are the upper and lower limits of the linear range. A linear range for the LEV is, when $u = v$, whereas, the saturation range for the LEV is when $u \neq v$. The control law for PI controller is expressed as

$$u = K_p \cdot e + K_i \cdot q \tag{19}$$

where K_p and K_i are the proportional and integral gains of the PI controller respectively. The q is the integral state. The error e is deviation of the actual speed with respect to the reference speed,which is expressed as

$$e = \omega_{ref} - \omega_m \tag{20}$$

The integral state q depends on the anti-windup scheme. The (23) presents the boundaries of the non-linear range i.e., saturation range. The boundaries for linear range is given as

$$\begin{cases} B_h: & K_i \cdot q = -K_p \cdot e + U_h \\ B_l: & K_i \cdot q = -K_p \cdot e + U_l \end{cases} \tag{21}$$

Fig. 5(a) shows the PI plane and shaded portion represents the linear range of the system. If the operating point ($K_p.e$, $K_i.e$) of the system is outside the linear range, then the control input is saturated and the control input to the system is not consistent with the integral state. In this case, proportional action is activated effectively. However, in steady state the value of $K_p.e$ should be zero and the value of K_i*q is K_i*q_{ss}, which lies on the integral axis where q_{ss} represnets steady state error of integral state . In steady state, the value of the $K_i q_{ss}$ depends on the operating conditions, such as load torque. When the PI trajectory enters the linear range, the trajectory reaches zero error through integral state corresponds to the anti-windup scheme.

Fig. 5(b) presents the low and high frequency responses (Bode magnitude plot) of PMaSyRM's first order mechanical system. It is observed that the gain of the LEV in the low frequency region is higher for the PI control as compared to P control. The value of the gains is equal for both P and PI control above the value of the breakaway frequency point (ω_b). The magnitude is decreasing above the break frequency. Hence, PI controller may cause an overshoot because of the integration of the error value for frequencies greater than the break frequency. It is observed that the LEV operation in P control is good for the value of frequencies above the break frequency. Whereas the operation of PI control is good for frequencies lower than the break frequency as it ensures zero steady-state error. Fig. 6 presents the integrator anti-windup technique employed for speed control of PMaSyRM-driven LEV. The method employed for the anti-windup of the integrator is conditional integration. In this method, a switch is provided to perform the integral action. The operation of the switch depends on the output of the comparator. The on condition of the switch indicates the integration operation.

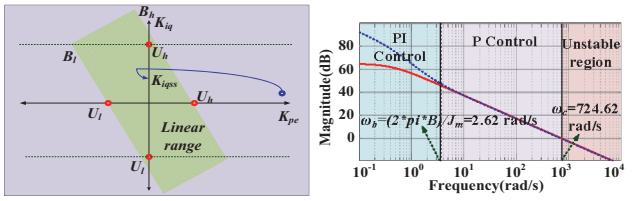

(a) (b)

Fig. 5. (a) Linear range and error trajectory in PI plane. (b) Frequency response of first order SYRM drive's mechanical system.

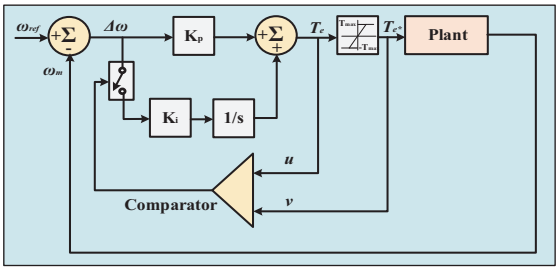

Fig. 6. Speed controller with integrator and conditional integration anti-windup technique.

Whereas, the off condition of the switch indicates integration operation is suspended. The switch remains in off condition when saturation of the controller occurs, and the sign of control error is the same as that of the sign of control signal. Here, the saturation of the controller means that the reference value of the torque is not equal to the unsaturated output of the PI controller. This method is called integrator clamping. Mathematically it is expressed as

$$\dot{q} = \begin{cases} e & u = v \\ 0 & u \neq v \end{cases} \tag{22}$$

The value of settling time t_s of the mechanical speed and the bandwidth ω_c of the speed controller are selected for the design of K_p and K_i values of the speed controller with anti-windup. The value of the bandwidth of the speed controller should be sufficiently greater than the mechanical time constant of the LEV. Based on the analysis, the values of K_p and K_i are calculated as [30]

$$K_p = J_m \cdot \omega_c \tag{23}$$

$$K_i = \frac{K_p \cdot \omega_c}{5} \tag{24}$$

IV. Results and Discussion

The proposed SPV and battery-integrated PMaSyRM-driven LEV system is simulated in Simulink. The anti-windup PI-based speed controller performance, BDDC performance while accelerating and regenerating, and operation of PMaSyRM are validated by simulating the integrated structure. The parameters of the SPV, BDDC and PMaSyRM are mentioned in the Appendices.

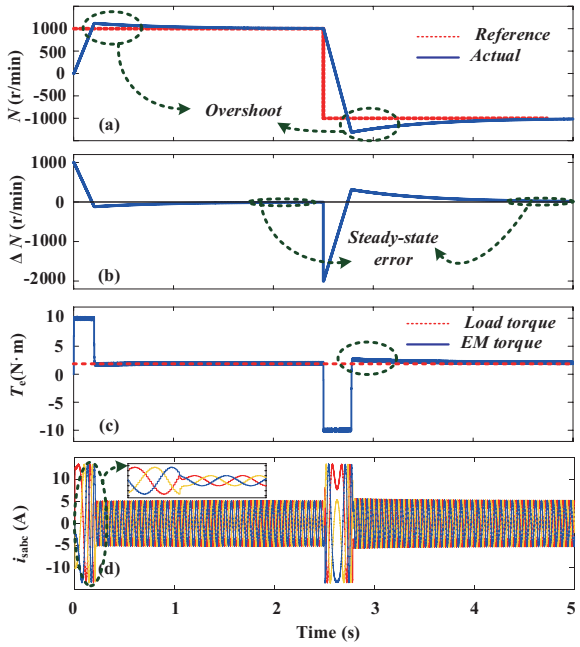

Fig. 7. Simulated results for conventional speed controller.

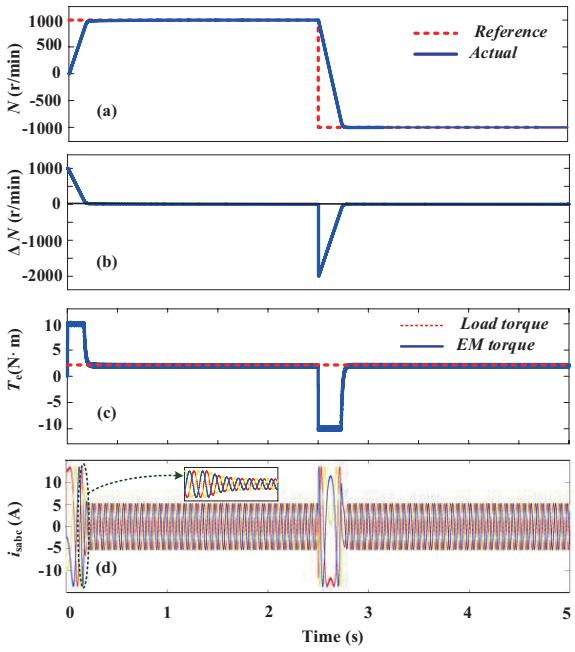

Fig. 8. Simulated results for speed controller with conditional anti-windup.

A. Comparative Analysis of Conventional Control and Proposed Integrator Anti-Windup Technique for the LEV

Figs. 7 and 8 presents the simulated results to verify the effectiveness of the conditional integration-based anti-windup technique of the speed controller. To validate the effectiveness of the anti-windup technique, PMaSyRM-driven LEV is started at zero speed with 2 N·m of load torque applied. The reference speed is given as 1000 r/min. At 2.5 s, the speed is reversed to −1000 r/min. Fig. 7 presents the results when the PMaSyRM-driven LEV is operated with a conventional speed controller. It is observed that there is an overshoot before the actual speed tracks the reference speed for conventional speed controller and it is observed that the overshoot occurs at the speed reversal as well. The steady-state error of 10 r/min is also observed after settling. The electromagnetic torque is also presented in N·m. It is observed that before settling to the reference speed, torque has overshoot. The overshoot is shown in the encircled area. The motor winding currents are also shown here. The effect of change in speed and hence oscillations are also observed in the winding currents as well. When the torque is at saturated value, the value of the winding currents is at 12.5 A. When the actual speed tracks the reference speed, the value of the current is equal to 4.7 A. In the enlarged view, it is observed that at the time of settling of the speed, the winding currents change abruptly.

Fig. 8 presents the results when the PMaSyRM driven LEV is operated with a conditional integration-based anti-windup technique. From Fig. 8(a), it is observed that there is no overshoot occurs and the actual speed tracks the reference speed within 0.2 s. Moreover, no steady-state error is observed. The error in speed tracking is also presented here. In the case of a conventional speed controller, apart from the same design of speed controller, the anti-windup technique is quite effective in controlling the PMaSyRM-based LEV for the overshoot and improvement in the steady state performance. This effectively increases the response and efficiency of the LEV.

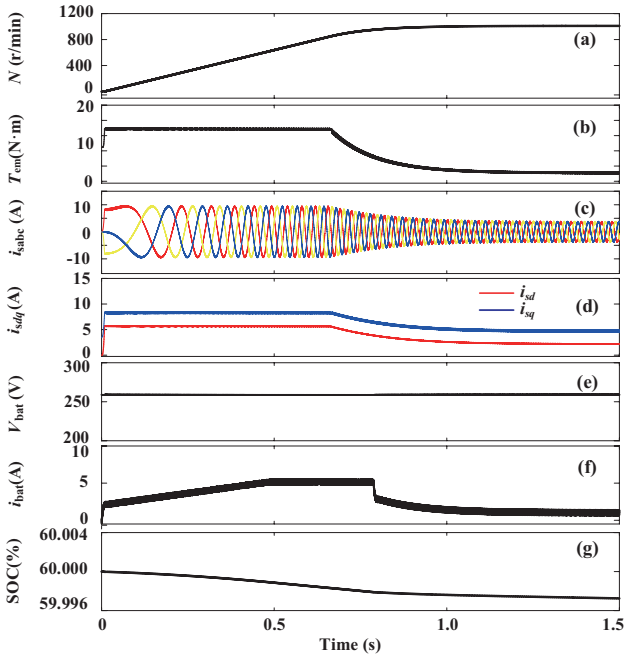

Fig. 9. Starting mode performance.

B. Starting and Acceleration Performance of PMaSyRM

Fig. 9 presents the starting performance of the SPV and battery-fed PMaSyRM drive controlled by the MTPA-based FOC technique. The load torque applied to the drive is 2 N·m. PMaSyRM drive starts from rest. The reference speed to the drive is 1000 r/min. When the drive starts from the rest, to

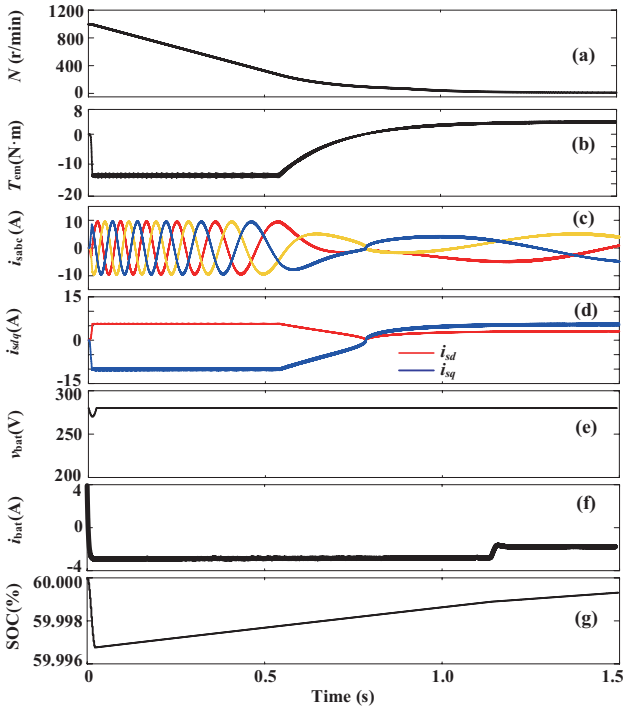

Fig. 10. Regenerative braking mode performance.

overcome the tractive forces acting on the drive, PMaSyRM electromagnetic torque goes into saturation, resulting in the acceleration of the drive. This is visible in Fig. 9(a)-(b). As shown in Fig. 9(c)-(d) effect of electromagnetic torque variation is visible in stator winding currents and *dq* component of the winding currents. The battery performance is presented in Fig. 9(e)-(g). The battery voltage remains consistent in magnitude throughout the operation of the PMaSyRM drive. However, while the drive is accelerating, battery gets discharged as battery current is positive in this case. The SOC of the battery also decreases when the drive is accelerating.

C. Regenerative Performance of PMaSyRM

Fig. 10 presents the regenerative mode performance of the PMaSyRM-based drive. To observe the regenerative performance of the drive, initially drive was operating at a speed of 1000 r/min with a load torque of 2 N·m applied to the drive. The reference speed is given as 10 r/min at 0.05 s. It is observed that as soon as the reference is given, the drive starts to decelerate. In the case of deceleration of the drive, the electromagnetic torque goes into negative saturation to overcome the tractive forces. Fig. 10(a)-(b) presents the speed and electromagnetic torque of the drive. While electromagnetic torque remains in saturation, the winding currents also attain the maximum allowable value. Fig. 10(c) shows that, while the drive is settled at 10 r/min with load torque of 2 N·m, the frequency of the winding current is also decreased. While deceleration of the drive, the *q*-axis component of the current goes into negative saturation. Fig. 10(d) presents the *dq* component of the winding currents. Fig. 10(e)-(g) presents the performance of the battery while regeneration operation of the

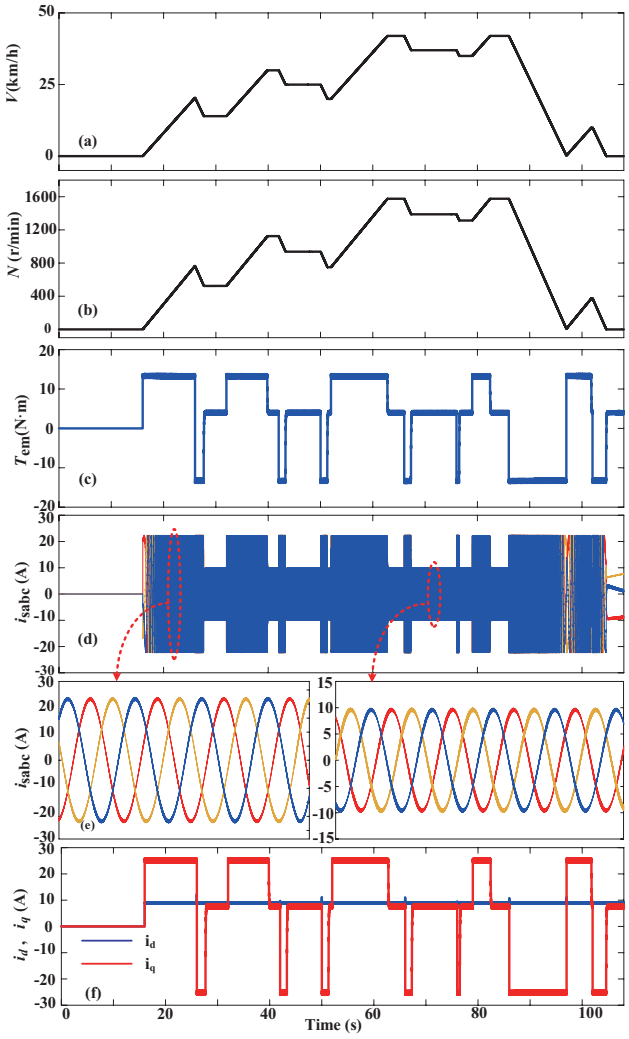

Fig. 11. (a) Vehicle dynamics: reference velocity. (b) SYRM speed variations. (c) electromagnetic torque. (d) stator winding currents. (e) enlarged view of stator winding currents. (f) *dq* axes' currents.

PMaSyRM drive. The voltage of the battery remains consistent in magnitude throughout the operation of the drive as observed in Fig. 10(e). The battery current in this case is negative, which shows that the battery is charging as observed in Fig. 10(f). Also, in Fig. 10(g) it is observed that the SOC of the battery is increasing. This implies that the drive is regenerating and the battery is charging while the drive is decelerating.

D. Driving Cycle performance

Fig. 11 and Fig. 12 present the Indian driving cycle-based performance of overall control structure and PMaSyRM driven LEV. Fig. 11(a) presents the single cycle of vehicle dynamics for Indian driving cycle. The duration of a single cycle is 108 s. During this 108 s, the maximum velocity attained by the LEV is 42 km/h. The vehicle parameters of LEV are presented in the Appendices. The speed of SYRM drive in RPM is presented in Fig. 11(b). The electromagnetic torque of the PMaSyRM drive is presented in Fig. 11(c). The gear ratio for the motor wheel drive system is considered as 3:1. It is observed that when

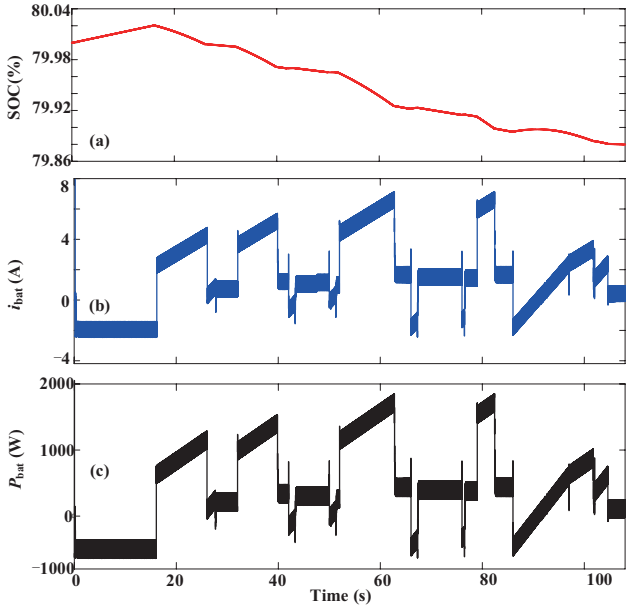

Fig 12. Battery dynamics: (a) battery SOC, (b) battery current, (c) battery power.

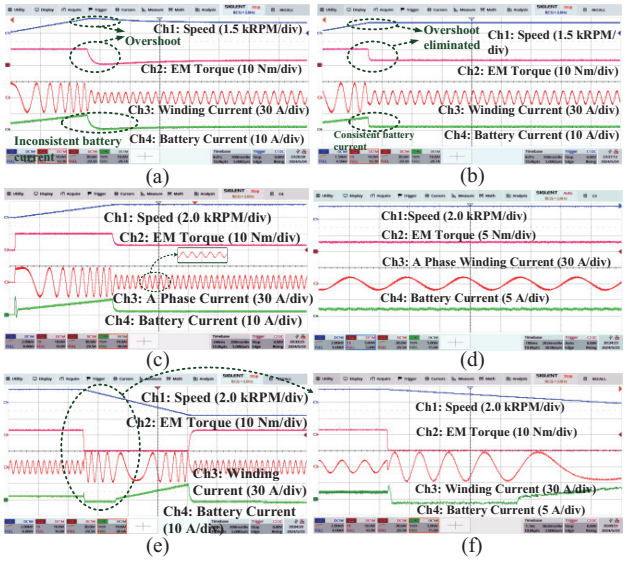

Fig. 13. (a)-(b) Starting performance of the conventional and anti-windup PI-controlled PMaSyRM drive (N_m, T_e, i_{sa}, i_b), (c) Starting performance of the anti-windup controlled PMaSyRM drive (N_m, T_e, i_{sa}, i_b), (d) Steady-state performance of the PMaSyRM drive (N_m, T_e, i_{sa}, i_b), (e)-(f) Dynamic performance and regeneration moment of the PMaSyRM drive (N_m, T_e, i_{sa}, i_b).

PMaSyRM drive is accelerating, the electromagnetic torque is in positive saturation, whereas, when vehicle is decelerating, the electromagnetic torque is negative saturation. Fig. 11(d) presents the stator winding currents of the PMaSyRM. Effects of variation in electromagnetic torque is observed in the stator winding currents. It is observed in the enlarged view of the stator winding currents, that when electromagnetic toque is in saturation, the positive and the negative peak of the winding current is +25 A and −25A respectively. Whereas, when the LEV is cruising positive and negative peak of the winding current is +10 A and −10 A respectively. Fig. 11(f) presents the *dq* axes' currents. It is observed that i_d is maintained at reference value of 9 A throughout the operation of the PMaSyRM drive. As, 9 A is given as the reference value to the PMaSyRM drive to maintain a constant flux in the drive. It is observed that *q*-axis current is following the reference electromagnetic torque command. The value of the i_q is positive when the electromagnetic torque is positive, whereas it is negative when the value of the electromagnetic torque is negative. Fig. 12 presents the performance of the battery and the BDDC. For motoring operation BDDC operates in the boost mode, whereas, for deceleration or braking BDDC operates in the buck mode. The charging of the battery occurs when the battery current is negative and SOC is increasing, whereas, discharging of the battery occurs when the battery current is negative, and SOC is decreasing. Battery SOC is presented in Fig. 12(a). Fig. 12(b) presents the battery current, and Fig. 12(c) presents the battery power. In the results, it is considered that LEV is in rest for 16 s and the SOC of the battery is 80%. The BDDC maintains the DC link voltage at 400 V. In these 16 s, it is considered that 1000 W/m^2 of solar insolation is available. Hence, S-PV transfers the power to the battery and charges the battery. It is observed that charging of the battery is reflected by the negative battery current. This phenomenon is accompanied by the increment in the SOC of the battery. It is observed from Fig. 12(b) that whenever vehicle is accelerating or cruising, the battery current is positive. Whereas, whenever brakes are applied, the battery current is negative and the SOC of the battery increases. Fig. 12(c) presents the battery power. It is seen that the power of the battery is positive whenever power is transferred from the battery to the PMaSyRM-driven LEV. Whereas the battery power is negative, whenever the power is transferred from the S-PV or braking of the drive to the battery.

V. Experimental Validation

The integrated SPV, BDDC and anti-windup PI speed controller based PMaSyRM drive is executed in the real time using OPAL-RT simulator. The OP4510 digital simulator is the core of the rapid control prototyping (RCP) system. The real time algorithm for the integrated system is created in MATLAB/Simulink software on the RT-LAB host computer. Along with the real time simulation, to verify the performance of the proposed system experiments are conducted on the prototype system developed in the laboratory. The system is prepared using a programmable solar PV emulator of 5 kW rating, a DC-DC boost converter, a gate-driver operated three-phase VSI, voltage and current sensors-based on Hall-effect principle, opto-couplers, dSpace DS 1202 controller and DC generator-coupled PMaSyRM.

A. Improved Performance of the Anti-windup Controlled PMaSyRM Driven LEV

The comparison of conventional PI controlled and anti-windup controlled PMaSyRM driven LEV is presented in Fig. 13(a) and (b) respectively. In Fig. 13(a), it is observed that there is an overshoot occurs in the speed waveform for a reference speed of 1000 r/min before settling to the reference

speed. The overshoot in the speed occurs at 1200 r/min. Also, it is observed that, PMaSyRM driven LEV takes time to settle to the reference speed. Effect of the overshoot in the speed, is also observed in the electromagnetic torque. It is observed that electromagnetic torque takes a dip before settling to load torque of 3 N·m. Because of this dip in the electromagnetic torque, the winding current magnitude also dips. This results in a delay in settling the winding current to a steady state. This phenomenon results in inconsistent battery current. The battery current takes longer to settle to a steady state. Fig. 13(b) presents the performance of an anti-windup controlled PMaSyRM drive. It is observed that the speed settles to the speed reference without any overshoot. The settling time of the speed is also less as compared to the conventional PI-controlled PMaSyRM drive. The electromagnetic torque also tracks the load torque smoothly without any dip. Since there is no dip in the electromagnetic torque, the winding currents also settle to the steady state value without any delay. This phenomenon results in consistent battery current, as battery current settles to the steady state value.

B. Starting Performance of the PMaSyRM Driven LEV

The starting performance of the EV is presented in Fig. 13(c). The starting performance of the drive reflects the acceleration part of the India driving cycle (IDC). In this case, EV is started from rest to top speed of the IDC i.e., 42 km/h, which is equal to 1600 r/min speed of the PMaSyRM, considering a gear ratio of 3:1 and wheel diameter of 400 mm. It is observed that PMaSyRM is tracking the speed smoothly, without any overshoot. It reflects that the PI controller with conditional integration anti-windup is working appropriately. Steady-state error also does not exist. The electromagnetic torque remains in saturation, while the drive is accelerating. Once the speed settles to the reference speed, torque is settled to the applied load torque of 3 N·m value. The effect of saturation in torque is seen in the stator winding currents of the PMaSyRM. The PMaSyRM draws a current of 30 A while, the drive is accelerating, once, the drive tracks the reference speed, the winding current's value comes down to the rated value. BDDC control is designed in such a way so that, in the acceleration or steady-state BDDC operates in boost mode and the battery current is positive, which indicates the transfer of power to the drive. It is observed that the current of the battery I_{bat}, from starting to the steady state of the drive is positive. At the start of the LEV, the battery draws a higher amplitude of current, once the drive settles to the reference speed, the battery current comes down to 2 A.

C. Steady-State Performance of the PMaSyRM Driven LEV

The steady state performance of the EV is presented in Fig. 13(d). In this case, EV is operating at constant speed of 42 km/h, which consists of constant acceleration according to the defined IDC. It is observed that PMaSyRM is operating at a constant speed of 1600 r/min, during the operation. Electromagnetic torque is maintained at 3 N·m of applied load torque. The stator winding currents of the PMaSyRM

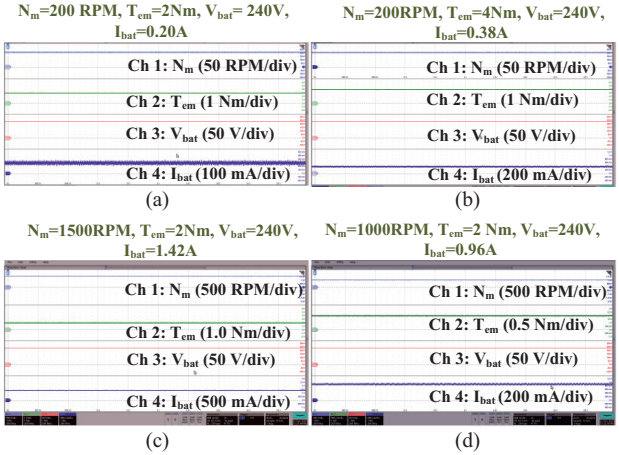

Fig. 14. (a)-(d) Steady state performance of the system for efficiency calculation (N_m, T_{em}, V_{bat}, I_{bat}).

is maintained throughout the steady-state operation of the PMaSyRM driven LEV. It is seen that the current of the battery is maintained at a constant positive value, which reflects that the current is supplied by the battery to transfer the power from the battery to the PMaSyRM driven LEV. BDDC control is designed in such a way that the BDDC, operates in the boost mode while supplying power from the battery to the PMaSyRM drive.

D. Dynamic Performance of the PMaSyRM Driven LEV

The dynamic performance of the integrated LEV is presented in Fig. 13(e)-(f). In this case, regeneration phenomenon of the system is verified. The PMaSyRM driven LEV operates at a speed of 1600 r/min, then a speed change of −1600 r/min is applied to the LEV. It is observed that the speed of the drive immediately starts decreasing, crosses zero speed and then tracks the set point of −1600 r/min. This phenomenon consists of deceleration as defined by the IDC. As the speed of the drive is decreasing, the electromagnetic torque goes into negative saturation. The effect of speed reversal and torque saturation is observed in the winding current as well. The current changes its phase as soon as the speed enters the negative speed zone from positive speed zone. From the battery current waveform, it is observed that battery current becomes negative from positive, as soon as the speed starts decreasing. The negative battery current reflects the charging operation of the battery. Hence, it is observed that deceleration in the speed, makes the BDDC to operate in the buck mode, and the power is transferred from the drive to the battery. The negative magnitude of the battery current is visible in the enlarged view of the speed reversal and regeneration phenomenon.

E. Steady State Performance for Efficiency Calculation

To analyse the overall efficiency of the system, experimental results are presented in Fig. 14. In Fig. 14 system is operated in the steady-state with the speed and load torque on the PMaSyRM is constant. This is done to analyze the efficiency of the system. In Fig. 14(a)-(d), the system is operated at

TABLE I
EFFICIENCY OF THE SYSTEM FROM BATTERY TO PMASYRM

N_m/(r/min)	T_{em}/(N·m)	V_{bat}/V	I_{bat}/A	P_{PMM}/W	P_{bat}/W	η_{bat_PMM}/%
200	2	240	0.20	41.87	48	87.22
200	3	240	0.29	62.80	69.6	90.23
200	4	240	0.38	83.73	91.2	91.81
500	2	240	0.48	104.67	115.2	90.86
500	3	240	0.71	157.00	170.4	92.14
500	4	240	0.92	209.33	220.8	94.81
1000	2	240	0.96	209.33	230.4	90.86
1000	3	240	1.43	314.00	343.2	91.49
1000	4	240	1.88	418.67	451.2	92.79
1500	2	240	1.42	314.00	340.8	92.14
1500	3	240	2.15	471.00	516	91.28
1500	4	240	2.78	628.00	667.2	94.12

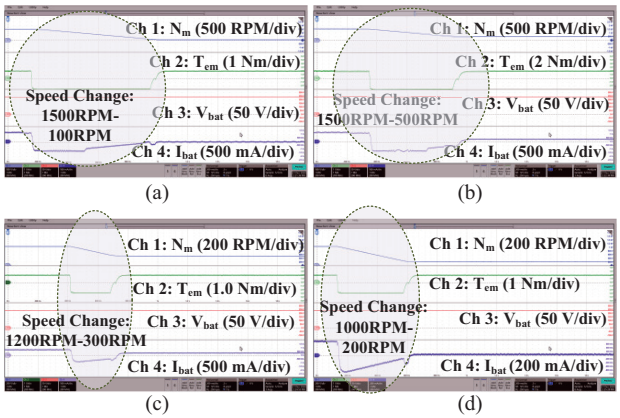

Fig. 15. (a)-(d) Regenerative braking operation of PmaSyRM (N_m, T_{em}, V_{bat}, I_{bat}).

speeds of 200, 200, 1500, and 1000 r/min respectively. For these speeds load torque of 2 N·m and 4 N·m applied on the PMaSyRM. Based on the results obtained in the steady state Table I is formed. To calculate the efficiency η_{bat_PMM} of the system from battery to PMaSyRM is calculated as follows:

$$\eta_{bat\_PMM} = \frac{T_{em} \times N_m \times 2\pi}{V_{bat} \times I_{bat} \times 60} \times 100\% \tag{25}$$

From Table I it is observed that the system's efficiency is well maintained in the range of 87.22% at 200 r/min to 94.12 at 1500 r/min. At low speed and low torque efficiency is slightly on the low side but maintained at 87.22%, however, at rated speed and slightly higher torque efficiency of the system increases to 94.12%. It implies that the from efficiency point of view system is working fine.

F. Efficicency of the Regenerative Braking Energy Recovery

Experimental results are presented in Fig. 15 to analyze the recovery of regenerative braking energy recovery. In Fig. 15(a)-(d), the machine is decelerated for a range of speeds. A summary of the range of speed change operations is presented in Table II. In Table II N_{mavg} is the average speed. The efficiency of the regenerative operation is calculated as

TABLE II
EFFICIENCY OF THE REGENERATIVE BRAKING ENERGY RECOVERY

Initial Speed /(r/min)	Final Speed /(r/min)	Avg Speed (N_{mavg}) /(r/min)	T_{em}/(N·m)	V_{bat}/V	I_{bat}/A	η_{regen}/%
1500	100	800	−3	240	−0.98	93.63
1500	500	1000	−3	240	−1.18	90.19
1500	1000	1250	−3	240	−1.21	88.66
1200	300	750	−3	240	−0.80	81.53
1000	200	600	−3	240	−0.71	89.17
800	200	500	−3	240	−0.58	88.86
1200	600	900	−3	240	−1.08	94.27
1200	400	800	−3	240	−0.92	89.91

$$\eta_{regen} = \frac{T_{em} \times N_{mavg} \times 2\pi}{V_{bat} \times I_{bat} \times 60} \times 100\% \tag{26}$$

From Fig. 15 and Table II, it is observed that the value of T_{em} and I_{bat} is negative. The negative sign of the torque implies that the machine is decelerating, whereas the negative sign of the battery current implies the charging of the battery. From Table II it is observed that efficiency is well above 85% for most of the speed changes. It implies that the energy which was previously got wasted in the braking, by usage of the regenerative mechanism and BDDC can be recovered. The efficiency of the regenerative braking mechanism is also satisfactory.

G. Comparison of Traditional LEV and Proposed LEV

As mentioned in the Appendix of the manuscript, battery voltage V_{bat} is considered as 240 V, battery ampere-hour rating is considered as 42 Ah. By considering 70% as the depth of discharge of the battery, total energy available from the battery is calculated as

$$E_{bat} = 240 \times 42 \times 0.7 = 7056 \text{ Wh} \tag{27}$$

As calculated 7056 Wh is the total power available from the battery for 1 hour of operation. As per the IDC, out of 108 s of operation of the LEV, brakes are applied for approximately 36 s. If it is considered that 1.5 kW of PMaSyRM of LEV operates at 350 W for one hour then, energy recovered by the battery through regenerative braking for 10 hours of daily operation of the LEV is calculated as

$$E_{regern} = \frac{350 \times 36 \times 10}{108} \approx 1166 \text{ Wh} \tag{28}$$

Hence 2500 Wh is the power available through the regenera-

TABLE III
COMPARISON OF TRADITIONAL LEV AND PROPOSED LEV

Energy Source	Conventional LEV	Proposed Work
Battery	7056 Wh	7056 Wh
Regenerative Braking	0 Wh	1166 Wh
PV Panel	0 Wh	2600 Wh
Net Power	7056 Wh	10822 Wh
For 95 kms of daily operation Energy available/km is	7056/95=74.27 Wh/km	10822/95=113.9 1 Wh/km
Range extension considering a single charge of the battery	7056/74.27= 95 km	10822/74.27=14 5 km

tive braking for 10 hours of daily operation of the LEV. As mentioned in the Appendix PV peak power available from the rooftop mounted PV panel is considered 650 W. Considering only 50% of the power is available for 10 hours of operation, 80% as the fill factor of the PV panel, and 20% as the losses, the net power available from the rooftop-mounted PV panel is calculated as

$$E_{\text{pv}} = 650 \times 0.5 \times 0.8 \times 10 = 2600 \text{ Wh} \tag{29}$$

Based on these calculations, Table III is formed to make a comparison of conventional LEV operation and proposed LEV operation from the prospect of available energy and range. From table III it is observed that for a single charge of the battery, traditional LEV can run up to 95 km, whereas, with the aid of regenerative braking and PV power, the proposed PV-battery-fed LEV can run up to 145 km. Hence calculation shows that the range in the case of the proposed LEV is extended as compared to the traditional LEV.

VI. CONCLUSION

This work presents the development of a PMaSyRM drive for an EV, integrating an SPV array and battery for energy regeneration. The LEV drive system is designed to enable battery charging through both regenerative braking and the SPV panel. The implementation of a conditional integrator-based anti-windup technique for speed control effectively eliminates ringing and overshoot during speed transitions, as demonstrated in the results. For better and optimized torque control MTPA technique is applied to generate the reference current set. The system's performance was tested using a standard IDC, with battery charging achieved via regenerative action and rooftop mounted SPV array. Throughout all vehicular modes, the stator currents supplied by the VSI remained within operating limits. The integrated system offers a practical solution for EVs, providing key advantages such as driving range extension, reduced operating costs, smooth speed and torque control, safe operation of the PMaSyRM and an extended battery life cycle. Additionally, charging the batteries via the SPV array enhances the affordability of EVs by expanding their range.

ACKNOWLEDGMENT

This work is supported by the IIT Bhilai with project Research Initiation Grant (RIG) and IBITF.

APPENDICES

Solar PV specifications: P_{mpp} = 650 Wp, V_{mpp} = 379.5 V, I_{mpp} = 1.8 A, V_{oc} = 400 V and I_{sc} = 2.0 A.

Battery Specifications: V_{bat} = 240 V, Rating =42 Ah, Li-ion battery.

BDDC Components: L = 5.6 mH, C_{dc} = 4000 μF.

Boost Converter Parameters: V_{in}= V_{mpp}=379.5 V, V_{out} = 400 V, L= 5 mH, Switching frequency (f_{s}) = 10 kHz.

PMaSyRM Specifications: Rated Power = 1.5 kW, V_{rated} = 230 V, I_{rated} = 7.5 A, R_{a} = 1.1 Ω, P = 4, L_d(sat)= 119.971 mH, L_q= 38.166 mH.

LEV specifications: Total weight = 480 Kg, turning radius = 2.9 m, drag coefficient = 0.45, rolling coefficient = 0.0143, and efficiency of transmission (in %) = 92%, wheel diameter= 400 mm.

REFERENCES

[1] I. Husain, B. Ozpineci, M. S. Islam, E. Gurpinar, G. -J. Su, W. Yu, S. Chowdhury, L. Xue, D. Rahman, and R. Sahu, "Electric drive technology trends, challenges, and opportunities for future electric vehicles," in *Proceedings of the IEEE*, vol. 109, no. 6, pp. 1039–1059, Jun. 2021.

[2] F. Momen, K. Rahman, and Y. Son, "Electrical propulsion system design of chevrolet bolt battery electric vehicle," in *IEEE Transactions on Industry Applications*, vol. 55, no. 1, pp. 376–384, Jan.-Feb. 2019.

[3] A. Babin, N. Rizoug, T. Mesbahi, D. Boscher, Z. Hamdoun, and C. Larouci, "Total cost of ownership improvement of commercial electric vehicles using battery sizing and intelligent charge method," in *IEEE Transactions on Industry Applications*, vol. 54, no. 2, pp. 1691–1700, Mar.-Apr. 2018.

[4] A. Stippich, C. H. Van Der Broeck, A. Sewergin, A. H. Wienhausen, M. Neubert, P. Schülting, S. Taraborrelli, H. Hoek, and R. W. De Doncker, "Key components of modular propulsion systems for next generation electric vehicles," in *CPSS Transactions on Power Electronics and Applications*, vol. 2, no. 4, pp. 249–258, Dec. 2017.

[5] X. Hu, J. Han, X. Tang, and X. Lin, "Powertrain design and control in electrified vehicles: A critical review," in *IEEE Transactions on Transportation Electrification*, vol. 7, no. 3, pp. 1990–2009, Sept. 2021.

[6] A. Latif, S. M. S. Hussain, A. Al-Durra, and A. Iqbal, "Hierarchical fuzzy framework for EV supported islanded microgrid frequency stabilization," in *IEEE Open Journal of the Industrial Electronics Society*, vol. 5, pp. 704–721, 2024.

[7] S. Chopra and P. Bauer, "Driving range extension of EV with on-road contactless power transfer—A case study," in *IEEE Transactions on Industrial Electronics*, vol. 60, no. 1, pp. 329–338, Jan. 2013.

[8] M. H. Mobarak and J. Bauman, "Vehicle-directed smart charging strategies to mitigate the effect of long-range EV charging on distribution transformer aging," in *IEEE Transactions on Transportation Electrification*, vol. 5, no. 4, pp. 1097–1111, Dec. 2019.

[9] B. Bilgin, J. Liang, M. V. Terzic, J. Dong, R. Rodriguez, E. Trickett, and A. Emadi, "Modeling and analysis of electric motors: state-of-the-art review," in *IEEE Transactions on Transportation Electrification*, vol. 5, no. 3, pp. 602–617, Sept. 2019.

[10] M. Ehsani, K. V. Singh, H. O. Bansal, and R. T. Mehrjardi, "State of the art and trends in electric and hybrid electric vehicles," in *Proceedings of the IEEE*, vol. 109, no. 6, pp. 967–984, Jun. 2021.

[11] B. Saha and B. Singh, "An adaptive delay compensated position sensorless PMBLDC motor drive with regenerative braking for LEV application," in *IEEE Transactions on Energy Conversion*, vol. 38, no. 3, pp. 1793–1802, Sept. 2023.

[12] S. S. Pasupuleti, N. R. Tummuru, and H. Misra, "Power management of hybrid energy storage system based wireless charging system with regenerative braking capability," in *IEEE Transactions on Industry Applications*, vol. 59, no. 3, pp. 3785–3794, May-Jun. 2023.

[13] S. Mishra, A. Varshney, B. Singh, and H. Parveen, "Driving-cycle-based modeling and control of solar-battery-fed reluctance synchronous motor drive for light electric vehicle with energy regeneration," in *IEEE Transactions on Industry Applications*, vol. 58, no. 5, pp. 6666–6675, Sept.-Oct. 2022.

[14] J. Lai, M. Chen, X. Dai, and N. Zhao, "Energy management strategy adopting power transfer device considering power quality improvement and regenerative braking energy utilization for double-modes traction system," in *CPSS Transactions on Power Electronics and Applications*, vol. 7, no. 1, pp. 103–111, Mar. 2022.

[15] A. K. Singh, A. K. Mishra, K. K. Gupta, and Y. P. Siwakoti, "High voltage gain bidirectional DC-DC converters for supercapacitor assisted electric vehicles: A review," in *CPSS Transactions on Power Electronics and Applications*, vol. 7, no. 4, pp. 386–398, Dec. 2022.

[16] O. Abdel-Rahim and H. Wang, "A new high gain DC-DC converter with model-predictive-control based MPPT technique for photovoltaic systems," in *CPSS Transactions on Power Electronics and Applications*, vol. 5, no. 2, pp. 191–200, Jun. 2020.

[17] N. Bianchi, S. Bolognani, E. Carraro, M. Castiello, and E. Fornasiero, "Electric vehicle traction based on synchronous reluctance motors," in *IEEE Transactions on Industry Applications*, vol. 52, no. 6, pp. 4762–4769, Nov.-Dec. 2016.

[18] F. N. Jurca, M. Ruba, and C. Marţiş, "Design and control of synchronous reluctances motors for electric traction vehicle," in *2016 International Symposium on Power Electronics, Electrical Drives, Automation and Motion (SPEEDAM)*, Capri, Italy, 2016, pp. 1144–1148.

[19] V. Prakht, V. Dmitrievskii, V. Kazakbaev, E. Valeev, A. Paramonov, and A. Anuchin, "Assessment of the feasibility of using a synchronous homopolar motor instead of an induction motor in a traction drive with a wide constant power speed range," in *IEEE Open Journal of Vehicular Technology*, vol. 5, pp. 950–966, 2024.

[20] A. E. Fitzgerald, C. Kingsley, and S. D. Umans, *Electric Machinery*, 6th ed., McGraw-Hill, New York, 2003.

[21] I. Boldea, L. N. Tutelea, L. Parsa, and D. Dorrell, "Automotive electric propulsion systems with reduced or no permanent magnets: An overview," in *IEEE Transactions on Industrial Electronics*, vol. 61, no. 10, pp. 5696–5711, Oct. 2014.

[22] S. Morimoto, Y. Takeda, T. Hirasa, and K. Taniguchi, "Expansion of operating limits for permanent magnet motor by current vector control considering inverter capacity," in *IEEE Transactions on Industry Applications*, vol. 26, no. 5, pp. 866–871, Sept.-Oct. 1990.

[23] S. Morimoto, M. Sanada, and Y. Takeda, "Wide-speed operation of interior permanent magnet synchronous motors with high-performance current regulator," in *IEEE Transactions on Industry Applications*, vol. 30, no. 4, pp. 920–926, Jul.-Aug. 1994.

[24] H. -B. Shin, "New antiwindup PI controller for variable-speed motor drives," in *IEEE Transactions on Industrial Electronics*, vol. 45, no. 3, pp. 445–450, Jun. 1998.

[25] J. -W. Choi and S. -C. Lee, "Antiwindup strategy for PI-type speed controller," in *IEEE Transactions on Industrial Electronics*, vol. 56, no. 6, pp. 2039–2046, Jun. 2009.

[26] J. Sun, Y. Yang, R. Chen, X. Zhang, C. S. Lim, and J. Rodriguez, "An efficient multi-vector-based model predictive current control for PMSM drive," in *CPSS Transactions on Power Electronics and Applications*, vol. 9, no. 1, pp. 79–89, Mar. 2024.

[27] W. Deng, J. Tang, and W. Cheng, "An enhanced rotating vector-based direct torque control for matrix converter-fed PMSM drives using virtual pulsating vectors," in *CPSS Transactions on Power Electronics and Applications*, vol. 8, no. 1, pp. 65–73, Mar. 2023.

[28] S. Kumar, A. Pandey, S. Singh, and S. Gupta, "Driving range extension of a PV array fed synchronous reluctance motor drive for electric vehicle with regeneration," in *2022 IEEE 10th Power India International Conference (PIICON)*, New Delhi, India, 2022, pp. 1–6.

[29] S. -Y. Jung, J. Hong, and K. Nam, "Current minimizing torque control of the IPMSM using Ferrari's method," in *IEEE Transactions on Power Electronics*, vol. 28, no. 12, pp. 5603–5617, Dec. 2013.

[30] J. -K. Seok, K. -T. Kim, and D. -C. Lee, "Automatic mode switching of P/PI speed control for industry servo drives using online spectrum analysis of torque command," in *IEEE Transactions on Industrial Electronics*, vol. 54, no. 5, pp. 2642–2647, Oct. 2007.

Sushant Kumar was born in Bhilai, India, in 1987. He received the B.E. degree in electrical engineering from the BIT, Bhilai, India, in 2009, and the M.Tech. degree in power systems and control engineering (Gold Medalist) from the National Institute of Technology, Raipur, India, in 2023. He is currently working toward the Ph.D. degree in electrical engineering with the Department of Electrical Engineering, Indian Institute of Technology Bhilai, Durg, India. From July 2009 to April 2020, he was an Assistant Manager with UltraTech Cement Limited and Aditya Birla Group. His research interests include control of electric drives and inverter design for drives.

Shailendra Kumar is currently working as an Assistant Professor in the Department of Electrical Engineering Indian Institute of Technology (IIT) Bhilai. He received the M.Tech and Ph.D. Degrees in PEEMD from the Indian Institute of Technology, Delhi, India, in 2015. He has also worked as an Assistant Professor at Maulana Azad National Institute of Technology, Bhopal from June 2020 to May 2023. His research interests include charging stations for EVs, power quality, grid integration of renewable energy resources, custom power devices, and microgrid. Dr. Kumar is recipient of prestigious POSOCO power system award (in Master as well as in Doctoral categories) in 2016 and 2019. He is also a recipient of Prof. Som Nath Mahendra Student Travel Awards for the IEEE PEDES 2018 conference and the IEEE UPCON Best Paper Award in 2016 and 2018. Dr. Kumar is a senior member of IEEE and member of INAE Societies.

Shashank Kurm is an Assistant Professor in the Department of Electrical Engineering at IIT Bhilai. He completed his Ph.D. from India Institute of Technology, Bombay, India in 2022, and Masters from India Institute of Science, Bengaluru, India in 2015. He has worked with L&T Technology Services where he has been involved in designing converters for electrical subsystems for automotive applications. His research areas and interests include high power density converters using wide band gap devices, multi-port converters for renewable and automotive applications, motor drives, and consumer electronics. He completed his bachelor's degree from National Institute of Technology, Raipur, India in 2013 and before joining for Ph.D., Dr. Kurm had a stint with CEA, Ministry of Power (India).